euspen's 22nd International Conference & Exhibition, Geneva, CH, May/June 2022
www.euspen.eu

Near-field spectroscopic measurement of thermally excited evanescent waves

Ryoko Sakuma[1*], Kuan-Ting Lin[2], Fuminobu Kimura[2], and Yusuke Kajihara [2, 3]

[1] *Department of Precision Engineering, The University of Tokyo, Hongo 7-3-1, Bunkyo-ku, Tokyo, 113-8656, Japan.*
[2] *Institute of Industrial Science, The University of Tokyo, Komaba 4-6-1, Meguro-ku, Tokyo, 153-8505, Japan.*
[3] *JST PRESTO, Honcho 4-1-8, Kawaguchi-shi, Saitama, 332-0012, Japan.*

**sakumar@iis.u-tokyo.ac.jp*

Abstract
Nano-thermography is essential for heat dissipation analysis, especially for nanoscale integrated circuits. However, development of widely applicable non-destructive nano-thermography is a challenging task due to the diffraction limit of the infrared waves. Recently, we have developed passive scattering-type scanning near-field optical microscopy (s-SNOM) that directly detects thermally excited evanescent waves with a spatial resolution of several tens of nanometers without using any external illuminations. The thermally excited evanescent waves are generated by local phenomena of materials including electron motions and lattice vibrations, and their energy density is determined by the electromagnetic local density of states and Bose-Einstein distribution. Since the signals obtained by the passive s-SNOM is determined by the local temperature, the passive s-SNOM has a great potential for nano-thermography. However, detailed thermal analyses including absolute temperature mapping and study of the local phenomena have not been realized due to the lack of a wavelength selection mechanism. To resolve this problem, we have developed a passive spectroscopic s-SNOM with grating-type spectroscopic mechanism. Here, we report the development of the passive spectroscopic s-SNOM and the near-field measurement of the thermally excited evanescent waves on metallic and dielectric materials. The passive THz spectroscopic s-SNOM was achieved using a blazed diffraction grating that was carefully designed to avoid mixing of light of different diffraction orders. It has more than 60 % and less than 8 % for the first and the second order diffraction efficiencies, respectively. We conducted a near-field detection of the thermally excite evanescent waves at several different wavelengths in the range of 14–15 μm with a wavelength resolution of 200 nm. From the decay feature of the detected signals, we verified that the detected near-field signals were not influenced by the external environment. The experimentally obtained signals were consistent with the calculated energy density.

Keywords: Measurement, Microscope, Optical, Scanning probe microscope (SPM), Nano-thermography

1. Introduction

Integrated circuits with nanosized structures are widely used in recent electronic devices. To reduce the energy consumption and improve the devise performance, it is important to study the heat transfer in nanoscale. Nanoscale thermography, including thermal atomic force microscopy (AFM) [1], fluorescent thermography [2], and quantum dot thermography [3], has been demonstrated for studying the local heat distribution. However, non-destructive and widely applicable nano-thermography is still a challenging task. Infrared thermography, which measures temperature using the spectrum of radiation waves from materials, has a high potential to be a widely used nano-thermography; however, its large spatial resolution due to the diffraction limit of light is a serious problem.

To resolve this problem, we have developed passive THz scattering-type scanning near-field optical microscopy (s-SNOM) [4]. It detects localized electromagnetic waves on a material surface, called thermally excited evanescent waves, with a spatial resolution of several tens of nanometers. The thermally excited evanescent waves are generated by uneven charge distributions due to local phenomena of materials including electron motions and lattice vibrations. The figure inset in Fig. 1(a) shows a schematic representation of the thermally excited evanescent waves. Its energy density is high near the material surface and exponentially decreases with distance from the surface. The total energy of the thermally excited evanescent waves is determined mainly by the material temperature and the electromagnetic local density of states (LDOS)[5]. Therefore, the intensity of the thermally excited evanescent waves can be used as a probe of the local temperature. Figure 1(a) displays a schematic of the passive THz s-SNOM. It consists of a charge sensitive infrared phototransistor (CSIP) [6], confocal optics, and a home-made AFM. The passive THz s-SNOM does not utilize any incident lights and thus directly detects radiation waves from samples. Using the passive THz s-SNOM, we have achieved detecting the ultra-small thermally excited evanescent waves without external illuminations. We have demonstrated nanoscale measurements of hot-electron energy dissipation [7] and Joule heating [8].

The passive THz s-SNOM has been achieved as a powerful nanoscale passive measuring technique; however, the lack of a wavelength selection mechanism limits the spectral analysis of the thermally excited evanescent waves. To deepen the understanding of the thermally excited evanescent waves and extend the range of applications, we have developed a passive THz spectroscopic s-SNOM with a wavelength selection mechanism. With the passive THz spectroscopic s-SNOM, absolute temperature mapping, surface analysis of condensed matter, and development of the passive detection theory would be realized. The principal aim of this study is to develop the passive THz spectroscopic s-SNOM and perform near-field detection of the thermally excited evanescent waves. Here we report two types of optical configurations for the spectroscopic

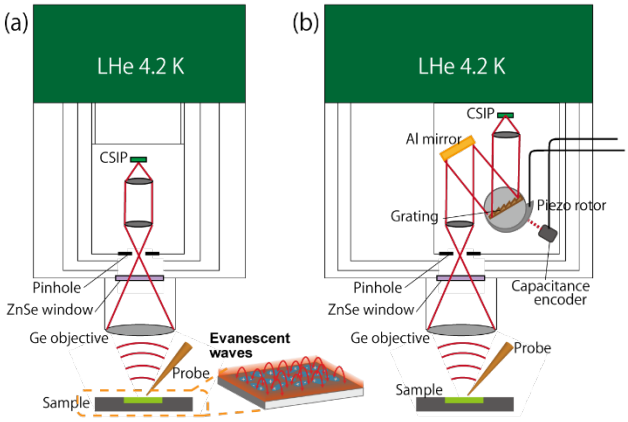

Figure 1. Schematics of (a) passive THz s-SNOM and (b) passive THz spectroscopic s-SNOM. The figure inset in Fig. 1(a) is a schematic of the thermally excited evanescent waves.

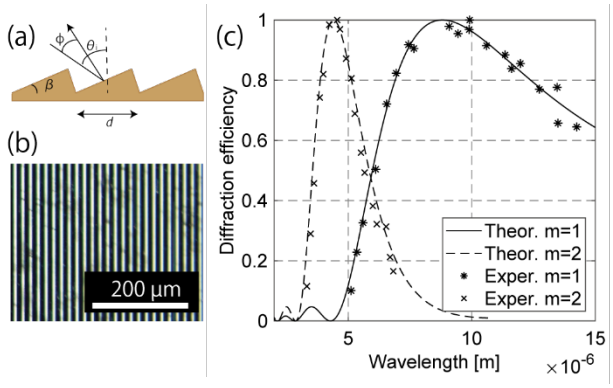

Figure 2. (a) Schematic of the blazed grating. (b) Microscopic image of the machiened grating. (c) Calculated and Experimental diffraction efficiencies. The solid line and the dashed lines represent the 1st and 2nd order calculated efficiencies and plots are the results of the FTIR measuremets.

mechanism and their optical performances. Using the developed passive THz spectroscopic s-SNOM, we detected the near-field signals on Au and SiC at a wavelength range of 14–15 μm. The detected near-field features were qualitatively consistent with the calculated electromagnetic local density of states (LDOS).

2. Development of the passive THz spectroscopic s-SNOM

2.1. Spectroscopy with a blazed grating

Figure 1(b) represents a schematic of the passive THz spectroscopic s-SNOM. The thermally excited evanescent waves are scattered by a probe and then a specific wavelength is selected by rotating a diffraction grating. The rotation angle is measured by a capacitance encoder. We intentionally selected the grating-based spectroscopy because it has a high signal efficiency and a simple mechanical movement for the wavelength selection mechanism. The simple mechanical movement is required because the spectroscopic system is operated at 4.2 K and thus makes the mechanical movement difficult due to an increase in friction and large energy losses.

The grating structure is shown in Fig. 2(a). It is a blazed grating with rectangular apexes. The grating pitch (d) is 15.5 μm and the blazed angle (β) is 17°. It was designed to have more than 60 % and less than 8 % of the 1st and 2nd diffraction efficiencies at a wavelength range of 8–16 μm, respectively. The diffraction wavelength and efficiency were calculated using the grating equation and the scalar theory of grating [9] shown in Eqs. (1) and (2).

$$\lambda = d/m\ (\sin\theta_i + \sin(\theta_i - \phi)) \qquad (1)$$

$$I = sinc^2\left(\frac{\pi d}{\lambda}\frac{cos\theta_i}{\cos(\theta_i-\beta)}\cdot[\sin(\theta_i-\beta)+\sin(\theta_i-\phi-\beta)]\right), \qquad (2)$$

where λ, d, m, θ_i, ϕ,and β are the diffraction wavelength, grating pitch, diffraction order, incident angle to the normal of the grating, angle between the incident and diffraction waves (30 °), and blazed angle, respectively. Figure 2(b) is the microscopic image of the blazed grating (material: Al alloy). It was machined rather than prepared by the metal deposition on a structural substrate to avoid the delamination between the different materials at an ultra-low temperature.

To experimentally verify whether the machined grating met the diffraction requirement, we measured the diffraction efficiency using Fourier Transform Infrared Spectroscopy (FTIR: Jasco, FT/IR-6600) [10]. The result is in Fig. 2(c). The solid and dashed lines are the 1st and 2nd order calculated diffraction efficiencies, respectively. The plots are the experimentally obtained diffraction efficiencies that are normalized to the maximum diffraction efficiency detected at a wavelength of 9.0 μm. The experimentally obtained efficiencies were normalized because the measurement condition of the passive THz s-SNOM and the sample chamber of FTIR are completely different. As shown in Fig. 2(c), the measured diffraction efficiency was consistent with the calculated values. The measurement precision was within 5 %.

2.2. Far-field spectroscopic performances with/without a mirror.

As described in Chapter 2.1, we introduced the spectroscopic optics with the blazed grating. The spectroscopic optics was with an Al mirror as shown in Fig. 1(b). Here, we introduce another optics configuration without the mirror. Figures. 3(a) and (c) are pictures of two different types of the optical configurations. Comparing to the conventional optics with the Al mirror, another optical configuration without the mirror has a 30% shorter optical path between the diffraction grating and the detector CSIP. Therefore, the influence of the misalignment of the grating position is minimized. Furthermore, the signal intensity is increased by approximately 10–20 % due to the absence of the absorption by the mirror, in principle.

To ascertain the optical response of these two optical configurations, we measured far-field spectra of a 500 K heat source. Here, we did not use the probe and detected the thermal radiation described by Planck's radiation law. The detector used for the measurement was a single-color CSIP (wavelength range: 14.5±0.8 μm). The final goal of this passive spectroscopy is with a wavelength range of 8-16 μm using a multi-color CSIP [11]; however, we have performed the spectroscopic analysis with the single-color CSIP due to its high sensitivity. Figures 3(b) and (d) represent the far-field spectra of a 500 K heat source using the optical configurations with and without the mirror, respectively. For both the optical configurations, a strong peak was observed at a wavelength of 0 μm. At this position, the incident angle to the normal of the grating was 15°; therefore, the 0th order diffraction light was obtained according to Eq. (1). Since light with all wavelengths are detected, we call this unique position as the broadband position. Furthermore, we can estimate the wavelength resolution from the FWHM of the peak at the broadband position. The wavelength resolutions calculated from Figs. 3(b) and (d) were approximately 200 nm and 150 nm, respectively.

At a wavelength range of 13–16 μm, a wider peak was observed. At this position, the signal was due to the 1st order diffraction light and light with a single wavelength was detected. Comparing to the intensity at the broadband position, the maximum signal intensities around a wavelength of 14.5 μm

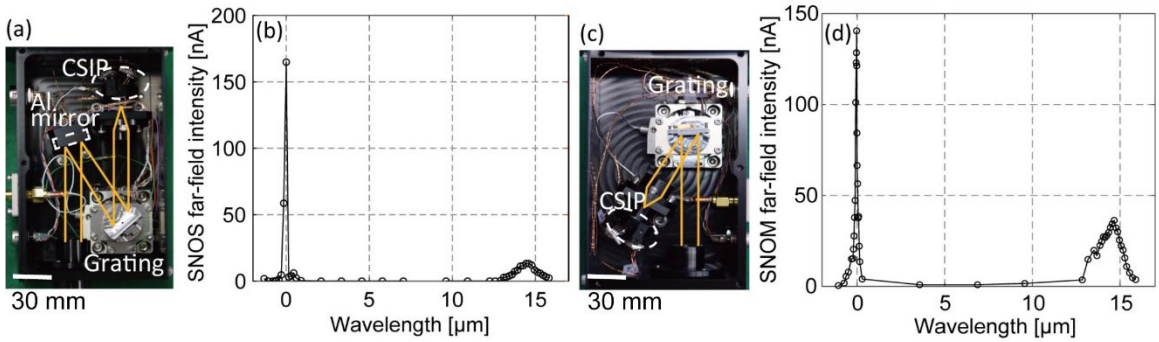

Figure 3. Pictures of the spectroscopic optics (a) with and (c) without the Al mirror for the passive THz spectroscopic s-SNOM. The far-field spectra of a 500 K heat source measured using the optics (b) with and (d) without the mirror. The strong peak at a wavelength of 0 μm is the 0th order siffraction light. The spectral range (the 1st order diffraction light) is 13–16 μm.

detected using the optical configurations with and without mirror were approximately 12 % and 28 % of that at the broadband position, respectively. As we described above, the decrease in the signal efficiency due to the misalignment of the grating was minimized using the optical configuration without the mirror. The signal intensity detected using the optical configuration without the mirror was smaller than that with the mirror at the broadband position. It was because of the difference in the position of the heat source and the deterioration of the grating surface.

3. Near-field measurements

3.1. 1D Near-field measurement on a SiC/Au sample

Then we performed near-field detection with the developed spectroscopic optics using a probe (material: tungsten). Using the probe, the electromagnetic waves just below the probe apex are propagated to the far field and detected. The spatial resolution is determined by the radius of the probe apex [12]. In our study, a probe with an apex radius of 20–100 nm was used. The probe was prepared by electrochemical etching. Figure 4(a) shows a schematic representation of the near-field scan. The probe is within 10 nm from the sample surface and vertically vibrated at a frequency of 11 Hz (Ω). The vertical vibration was applied to extract the near-field component. The mechanism of the near-field extraction is as follows: the thermally excite evanescent waves exponentially decay with distance, whereas the background electromagnetic waves are constant. Therefore, the probe was vibrated and the amplitude of the varying CSIP signal was extracted using a lock-in amplifier with a reference frequency of 11 Hz. The time constant of the lock-in amplifier was 10 s. The vibration amplitude depends on the materials.

Figure 4(b) is a microscopic image of the micro-patterned sample. A cross-patterned Au with a thickness of 100 nm is deposited on a SiC substrate. We performed 1D near-field scan along the arrow in Fig. 4(b). Figure 4 (c) shows the result of the 1D scan at the broadband position and a wavelength of 14.5 μm. The sample structure is represented in Fig. 4(c) inset. At both the broadband position and a wavelength of 14.5 μm, the near-field signal on Au is higher than that on SiC. The signal intensity detected at a specific wavelength is reduced to 1/10–1/5 of that at the broadband position due to the limited number of incident phonons. The 1D profile indicates that the spatial resolution is approximately 200 nm. Although the improvement of the signal to noise ratio (SNR) is required to perform a thorough spectroscopic analysis, we have achieved detecting the near-field signal of the thermally excited evanescent waves both at the broadband position and a specific wavelength.

3.2. Measurement of near-field decay on Au

The total energy of the electromagnetic waves above a material surface is described by [5]

$$u(z,\omega,T) = \rho \frac{\hbar\omega}{\exp\left(\frac{\hbar\omega}{k_B T} - 1\right)}, \quad (3)$$

where k_B, T , and ρ are the Boltzmann's constant, temperature, and the electromagnetic local density of states (LDOS). The electromagnetic LDOS can be calculated using fluctuation–dissipation theorem, which is described by;

$$\rho = \frac{\omega^2}{2\pi^2 c^3}\left\{\int_0^{\omega/c} \frac{KdK}{k_0|\gamma_1|}\frac{(1-|r_{12}^s|^2)+\left(1-|r_{12}^p|^2\right)}{2} + \int_{\omega/c}^{\infty} \frac{4K^3\,dK}{k_0^3|\gamma_1|}\frac{\mathrm{Im}(r_{12}^s)+\mathrm{Im}(r_{12}^p)}{2}\exp(-2\mathrm{Im}(\gamma_1)z)\right\}. \quad (4)$$

r_{12}^s, r_{12}^p, and c in Eq. (4) denote the Fresnel reflection factor for s and p polarization, and the speed of light in vacuum, respectively. k_0 and γ_1 are given by ω/c and $\varepsilon_1\mu_1 k_0^2 - K^2$where ε_1 and μ_1 are the dielectric constant and the magnetic constant of the material. We conducted the near-field detection at room temperature and assumed that the near-field signals detected at the CSIP is directly proportional to the electromagnetic LDOS. Figure 5(a) represents the calculated near-field decay feature of Au at a wavelength of 14.5 μm using Eq. (4). It indicates that the thermally excited evanescent waves are exponentially decreased, and the decay length is approximately 20 nm.

In order to clarify whether the detected near-field signals does not include artifact components, we measured the near-field decay feature. We moved the probe away from the sample surface by 3 nm at every 10 s and observed the change in the CSIP signal. We applied the vertical vibration with an amplitude of 100 nm to the probe to extract the near-field component. The figure inset of Fig. 5(a) is the schematic representation of the decay detection.

Many studies related to the active-type s-SNOM with external illumination indicated that the feature of the near-field decay detected at the fundamental frequency (Ω) has a longer tail because of artifact components [13, 14]. Most of the artifact components are the background scattering at the probe shaft. Therefore, the second ($2\,\Omega$) or third harmonics ($3\,\Omega$) are used to extract the near-field components. On the other hand, the passive measurement, which does not used any external illumination, does not require using the higher harmonics because the thermally excited evanescent waves are localized very close to the surface (z<100 nm) and there is no interaction between the evanescent waves and the probe shaft. As a result, the near-field decay detected at the fundamental frequency has a similar decay feature to that of calculated [15].

Figures 5(b)–(c) are the experimentally obtained near-field decay features (n=8) on Au at wavelengths of 14.2, 14.5, and 14.8 μm, respectively. The SNR of the near-field decay curve at

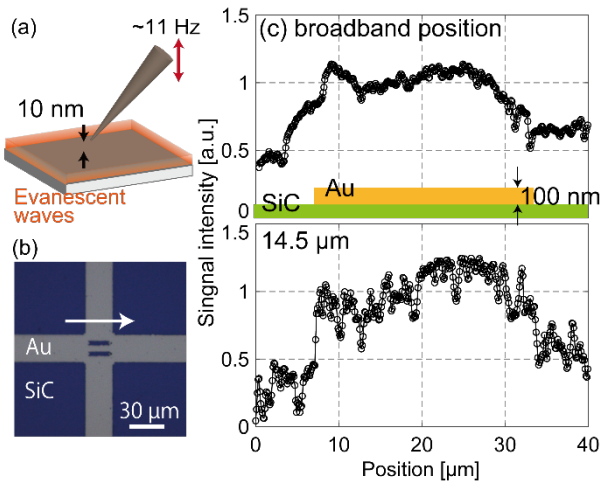

Figure 4. (a) A schematics representation of the scanning of the sample. (b) A microscopic image of the SiC/Au micro-patterned sample. (c) 1D scans of the near-field signals at the broadband position and a wavelength of 14.5 μm. The figure inset is a schematic of the sample structure.

a wavelength of 14.2 μm, shown in Fig. 5(b), is relatively low due to the low optical response at the edge of the spectral range of the passive THz spectroscopic s-SNOM. At all wavelengths in a range of 14.2–14.8 μm, we obtained the near-field decay curves that was similar to the calculated electromagnetic LDOS, shown in Fig. 5(a). The decay length of the near-field decay curve was about 25 nm at a wavelength of 14.8 μm, shown in Fig. 4(d), and that at wavelengths of 14.2 and 14.5 μm was approximately 50 nm, shown in Figs. 5(b) and (c). The longer decay length at wavelengths of 14.2 and 14.5 μm was due to the attraction of the probe tip to the sample surface by the atomic force between them, and the distance between the probe tip and the sample changed during the measurements. The change in decay length was not observed if the probe was moved faster away from the surface; however, the SNR decreased. The experimentally obtained near-field decay curves, which have similar decay features to that of calculated, indicate that the near-field signals detected at the fundamental frequency (Ω) does not include any artifact components induced by the external environment. The result clearly shows that the developed passive THz spectroscopic s-SNOM can directly detect the spectrum of the thermally excited evanescent waves.

Although the SNR of the near-field signal and the tip-sample attraction during the near-field measurement are needed to be improved, it was the first time that the near-field decay curve at a specific wavelength was passively detected. The rapidly decreasing near-field decay feature indicates that the detected near-field signals are not influenced by any external environments. Since the intensity of the thermally excited evanescent waves are determined by the electromagnetic LDOS and temperature as shown in Eq. (3), the developed passive THz spectroscopic s-SNOM can be applied to nano-thermography or passive-type chemical microscopy with a high spatial resolution of 10–100 nm.

4. Conclusion

In this study, we have developed passive THz spectroscopic s-SNOM and performed near-field measurements. The machined blazed grating with a pitch of 15.5 μm and a blazed angle of 17° achieved over 60 % of the 1 diffraction efficiency. We compared the far-field signal intensity in the spectral range (wavelength: 13–16 μm) relative to that at the broadband position using different optical configurations with and without the Al mirror.

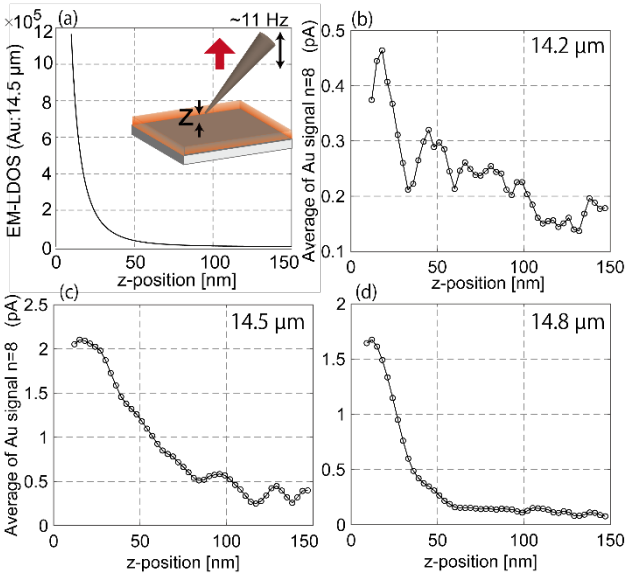

Figure 5. Decay profiles of the near-field signal. (a) The calculated decay profile of the near-field signal on Au at a wavelength of 14.5 μm. The figure inset is a schematic representation of the decay detection. The experimentally obtained near-field signals on Au at wavelengths of (b) 14.2 μm, (c) 14.5 μm, and (d) 14.8 μm.

The signal intensity in the spectral range detected using the optical configuration without the mirror showed 2.3-fold increase compared with that with the mirror. Using the developed spectroscopic mechanism, we performed 1D scan and decay-curve detection of the near-field signal at wavelengths of 14.2, 14.5, and 14.8 μm. From the 1D profile of the near-field signal, we have experimentally verified that the spatial resolution was approximately 200 nm. Moreover, the near-field decay features detected using a probe, which was vibrated at the fundamental frequency, indicated that the obtained near-field signals in the spectral range was not influenced by the external environment. The developed passive THz spectroscopic s-SNOM will be applied to a variety of passive spectroscopic measurements including nano-thermography and nano-chemical microscopy.

References

[1] Duvigneau J, Schönherr H, and Vancso G 2010 *ACS Nano* **4**(11) 6932-6940.
[2] Gao H, Kam C, Chou T Y, Wu M-Y, Zhao X, and Chen S 2020 *Nanoscale Horiz.* **5**(3) 488-494.
[3] Yang J-M, Yang H, and Lin L 2011 *ACS Nano* **5**(6) 5067-5071.
[4] Kajihara Y, Kosaka K, and Komiyama S *Rev. Scient. Instr.* **81**(3) 033706.
[5] Joulain K, Carminati R, Mulet J-P, and Greffet J-J 2003 *Phys. Rev. B* **68**(24) 245405.
[6] Ueda T, An Z, Hirakawa K, and Komiyama 2008 S *J Appl. Phys.* **103**(9) 093109.
[7] Weng Q, Komiyama S, Yang L, An Z, Chen P, Biehs S-A, Kajihara Y, and Lu W 2018 *Science* **360** 775-778.
[8] Weng Q, Lin K-T, Yoshida K, Nema H, Komiyama S, Kim S, Hirakawa K, and Kajihara Y 2018 *Nano Lett.* **18** 4220-4225.
[9] Casini R. and Nelson P G 2014 *J. Opt. Soc. Am. A* **31**(10) 2179-2186.
[10] Sakuma R, Lin K-T, Kim S, Kimura F, and Kajihara Y 2019 *IEEE Photon. Tecgnol. Lett.* **31**(15) 12261-1264.
[11] Kim S, Komiyama S, Ueda T, Satoh T, and Kajihara Y 2015 *Appl. Phys. Lett.* **107**(18) 182106.
[12] Lin K-T, Komiyama S, and Kajihara, Y 2016 *Opt. Lett.* **41**(3) 484-487.
[13] Hermann P, Hoerhl A, Patoka P, Huth F, Rühl E, and Ulm G 2013 *Opt. Exp.* **21**(3) 2913-2919.
[14] Knoll B, and Keilmann F 2000 *Opt. Commun*. **182** 321-328.
[15] Kajihara Y, Kosaka K, and Komiyama S 2011 *Opt. Exp.* **19**(8) 7695-7704.